

Synthesis and Characterization of Water-Soluble Conjugated Oligoelectrolytes for Near-Infrared Fluorescence Biological Imaging

Shin-Jae Woo,[†] Sungmin Park,[‡] Ji-Eun Jeong,[‡] Yoochan Hong,[§] Minhee Ku,^{§,||} Bo Yun Kim,[⊥] Il Ho Jang,[⊥] Soon Chul Heo,[⊥] Taejun Wang,[#] Ki Hean Kim,[#] Jaemoon Yang,^{*,§,||} Jae Ho Kim,^{*,⊥} and Han Young Woo^{*,‡}

[†]Department of Cogno-Mechatronics Engineering, Pusan National University, Miryang 50463, Republic of Korea

[‡]Department of Chemistry, Korea University, Seoul 02841, Republic of Korea

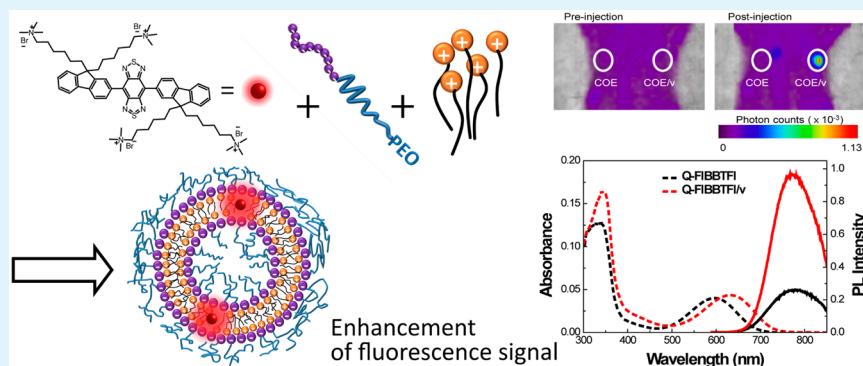
[§]Department of Radiology, College of Medicine, Yonsei University, YUHS-KRIBB Medical Convergence Research Institute, Seoul 03722, Republic of Korea

^{||}Brain Korea 21 PLUS Project for Medical Science, Yonsei University, Seoul 03722, Republic of Korea

[⊥]Department of Physiology, School of Medicine, Pusan National University, Yangsan 50612, Republic of Korea

[#]Division of Integrative Biosciences and Biotechnology, Department of Mechanical Engineering, Pohang University of Science and Technology, Pohang 37673, Republic of Korea

S Supporting Information



ABSTRACT: Near-infrared (NIR) fluorophores attract increasing attention as a molecular marker (or probe) for in vivo and in vitro biological fluorescence imaging. Three types of new NIR fluorescent conjugated oligoelectrolytes (COEs: Q-FITBTFl, Q-FIBBTFl, and Q-FITBBTFl) are synthesized with quaternized ammonium ionic groups in their side-chains for water solubility. The emission wavelength is modulated in the range 600–1300 nm, by adjusting the intramolecular charge transfer in the molecular backbone based on the electron-rich fluorene (and/or thiophene) and electron-deficient benzo[2,1,3]thiadiazole (or benzo[1,2-*c*:4,5-*c'*]bis[1,2,5]thiadiazole) moieties. The COEs show a remarkably larger Stokes shift (147–276 nm) compared to commercial rhodamine and cyanine dyes in water, avoiding self-quenching and interference from the excitation backscattered light. The photoluminescence (PL) quantum efficiency is improved substantially by up to 27.8% in water by fabricating a vesicular complex, COE/v, with a block ionomer, poly[(ethylene oxide)-*block*-(sodium 2-acrylamido-2-methyl-1-propane-sulfonate)]. In vitro cellular uptake images with the COEs are obtained with good biocompatibility by confocal single-photon and two-photon microscopy. The ex vivo and in vivo images of a mouse xenograft model treated with the Q-FIBBTFl/v exhibit a substantially stronger fluorescence signal at the tumor site than at the other organs, highlighting the potential of the COE/v as an NIR fluorescent imaging agent for the diagnosis of cancer.

KEYWORDS: conjugated oligoelectrolytes, near-infrared fluorophores, vesicle, Stokes shift, bioimaging

1. INTRODUCTION

The development of fluorescent probes for bioassays with the visualizing targets of interest, both in vitro and in vivo, has been encouraged to unveil a range of biological events.^{1–7} In particular, near-infrared (NIR) fluorophores, which emit in the range of 650–900 nm, the so-called “biological window”, are of great importance for potential applications in in vivo biological

imaging, because of several advantages including deep tissue penetration of NIR light, minimal interference from the background signals (because of the negligible autofluorescence

Received: April 11, 2016

Accepted: June 7, 2016

Published: June 7, 2016

of biomolecules), low light scattering, less photodamage to biological samples, etc.^{8–16} Despite the extensive research on the molecular design, synthesis and optical characteristics, fluorescent sensors, and imaging applications of visible light-emitting fluorophores, relatively few NIR fluorescent structures have been reported, including rhodamine, 4,4-difluoro-4-bora-3a,4a-diaza-s-indacene dyes (BODIPY), squaraine, and cyanine derivatives.^{17–21} As those NIR fluorophores show several limitations, i.e., poor water solubility and low fluorescence quantum efficiency in water, low photostability, undesired intracellular localization (or poor cell permeability), small Stokes shift, etc., new searches for brilliant water-soluble NIR fluorescent alternatives to overcome those concerns are of great interest.^{22–24}

Recently, there has been growing attention in conjugated oligoelectrolytes (COEs), which are delocalized π -conjugated molecules with ionic functionalities. Many potential applications in organic electronic devices, bioimaging, biosensors, and bioelectronics systems have been identified owing to their useful electrical and optical properties and water solubility.^{25–30} COEs with conjugated electron donor (D) and acceptor (A) moieties in their backbone exhibit broad, strong, and red-shifted absorption/emission with a large Stokes shift via intramolecular charge transfer (ICT) interactions.^{31–33} Their absorption and photoluminescence (PL) characteristics can be tuned easily by adjusting the ICT through the appropriate choice of electron-rich and poor D/A pairs. Finally, the fine adjustment of electron-donating and -accepting ability in the D–A molecular framework controls the bandgap of the resulting fluorophores. For water solubility, positive or negative ionic groups are often attached as side-chains. The PL wavelength and quantum efficiency of D–A type COEs are sensitive to the solvent polarity, suggesting the potential use of COEs as a microenvironment probe in biological media.^{34,35}

This paper reports the synthesis and photophysical characterization of three kinds of water-soluble NIR COEs and their application to in vitro and in vivo NIR fluorescence (NIRF) imaging. The COEs showed absorption and PL spectra in the range 300–1000 nm and 600–1300 nm in water, respectively, depending on the ICT interactions in their molecular structures based on fluorene, thiophene, benzothiadiazole, and benzobis-thiadiazole moieties. The COEs also showed a remarkably larger Stokes shift (147–276 nm in water) compared to commercial rhodamine and cyanine dyes. By increasing the ICT interactions, the absorption and emission spectra were red-shifted, showing a gradual decrease in PL quantum efficiency in both toluene (77 \rightarrow 13.1%) and water (5.7 \rightarrow \sim 0.1%) due to the energy gap law.³⁶ The COEs were also incorporated in a polymeric vesicle (COE/v) to improve the PL efficiency via microenvironment modulation near the COEs in water,³⁷ showing substantially improved PL efficiency (1.2–27.8%). The COEs and COEs/v showed a good biodistribution, low cytotoxicity, and good passive targeting for tumor cells in the mouse model, highlighting their potential as NIR in vivo imaging agents.

2. EXPERIMENTAL SECTION

2.1. General. 1,2,4,5-Tetraaminobenzene tetrahydrobromide (95% purity) was purchased from Hangzhou Trylead Chemical Technology Co., Ltd. All other chemical reagents were obtained from Aldrich Chemical Co., Junsei Chemical Co., or Tokyo Chemical Industry Co., Ltd. 4,8-Dibromobenzo[1,2-*c*:4,5-*c'*]bis[1,2,5]thiadiazole (1), 4,7-dibromobenzo[2,1,3]thiadiazole (2), and 2-bromo-9,9-bis(6'-

bromohexyl)fluorene (3) were synthesized using the reported procedures.^{38–40} The ¹H and ¹³C nuclear magnetic resonance (NMR) spectra were recorded on a JEOL (JNM-AL300) FT-NMR system operating at 300 and 75 MHz, respectively. The mass spectra were recorded using a Bruker ultraflex extreme matrix-assisted laser desorption ionization time-of-flight (MALDI-TOF) mass spectrometer. The dynamic light scattering (DLS) and zeta-potential measurements were performed using a Malvern Zetasizer Nano-ZS instrument. Cyclic voltammetry (CV) measurements (Versa STAT 3 analyzer, AMETEK) were carried out in 0.1 M tetrabutylammonium tetrafluoroborate (Bu₄NBF₄) in acetonitrile with a conventional three-electrode configuration employing a platinum wire as a counter electrode, platinum electrode as a working electrode, and Ag/Ag⁺ electrode as a reference electrode. The UV–vis absorption spectra were measured using a Jasco (V-630) spectrophotometer. The photoluminescence (PL) spectra were obtained on a HORIBA (Fluorolog-3) spectrofluorometer with a xenon lamp as the excitation source using a 90° angle detection for the solution samples. The PL quantum efficiency (Φ_{PL}) was determined relative to indocyanine green (ICG) (Φ_{PL} = 0.13 in dimethyl sulfoxide), rhodamine 101 (Φ_{PL} = 0.96 in ethanol), and fluorescein (Φ_{PL} = 0.92 in phosphate buffered saline (PBS), pH = 10) as a standard.

2.2. Vesicular complex formation. Synthesis and characterization of poly[(ethylene oxide)-*block*-(sodium 2-acrylamido-2-methyl-1-propanesulfonate)] (E₄₅-A₇₀) were reported in our previous report.³⁷ Briefly, the vesicular complex (COE/v) containing the NIR COEs was prepared in water as follows.³⁷ An aqueous E₄₅-A₇₀ (0.5 mM, stock solution) solution (20 μ L) was added to an aqueous solution of NIR COE (5 μ M, 2 mL) in a cuvette ($[E_{45}\text{-}A_{70}] = 5 \mu\text{M}$), and the required amount (until saturation of PL intensity change) of aqueous hexadecyltrimethylammonium bromide (C₁₆) solution (5 mM, stock solution) was added into the above mixture ($[C_{16}] = 375 \mu\text{M}$). The vesicular complex formation was completed around a charge ratio ($[-] = 70 \times 5 \mu\text{M} = 350 \mu\text{M}$ in E₄₅-A₇₀; $[+] = (4 \times 5 \mu\text{M}$ in COE + 375 μM in C₁₆ = 395 μM) of \sim 1:1, at which the highest PL signal was measured for COE/v.

2.3. Cell culture. Human embryonic kidney 293 cells were cultured in a high glucose–Dulbecco's modified Eagle's medium (DMEM) medium supplemented with 10% fetal bovine serum (FBS) and 1 \times penicillin-streptomycin. Mouse embryonic fibroblasts (MEFs) were isolated from E13.5 CF1 mouse embryos after removing the brain and visceral tissue and maintained in MEF medium (DMEM with high glucose, 1 \times Glutamax-1, 10% FBS, and 1 \times penicillin-streptomycin). Human endothelial progenitor cells (EPCs) were isolated from human umbilical cord blood and maintained in endothelial cell basal medium-2 (EBM-2) (Clonetics, San Diego, CA) supplemented with EGM-2 MV SingleQuots containing 5% FBS, human VEGF-1, human fibroblast growth factor-2, human epidermal growth factor, insulin-like growth factor-1, and ascorbic acid.

2.4. Confocal single-photon and two-photon microscopy. Single-photon and two-photon microscopy images of EPCs were acquired after incubation with 10 μ M of Q-FITBTTFI for 12 h. A custom-designed confocal laser scanning microscope for single- and multiphoton imaging (TCS SP5 II, Leica) with both 514 nm argon laser and IR-tunable Ti:Sapphire laser (Chameleon Vision II, Coherent) was used. The excitation and emission spots were raster-scanned in 0.5 mm steps over the selected regions of interest to generate the emission wavelength scans. A two-photon excitation laser (140 fs pulse width, 80 MHz repetition rate) was tuned to 1100 nm, and the emission signals were acquired using nondescanned detectors by splitting a long-pass dichroic filter LP 620. A mean laser power at the cell surface was \sim 5–20 mW depending on the depth of recording and the field of view. The 12-bit two-photon fluorescence images were acquired with a spatial resolution of 1024 \times 1024 pixels and a scan speed of 400 Hz. Image processing was performed using LAS AF Lite (Leica, Germany).

2.5. In vivo and ex vivo fluorescence imaging. In vivo and ex vivo NIR fluorescence imaging was conducted using an eXplore Optix system (ART Advanced Research Technologies). A solution containing the NIR COE or its vesicular complex was prepared in a

1.5 mL centrifuge tube. The laser power and count time settings were optimized at 0.04 μW , and the temporal point spread function integration time was set to 1 s per point. The excitation and emission spots were raster-scanned in 0.5 mm steps over the selected regions of interest to generate the emission wavelength scans. The filter sets used were $\lambda_{\text{ex}} = 665 \text{ nm}/\lambda_{\text{em}} = 693 \text{ nm}$. All animal experiments were conducted with the approval of the Association for Assessment and Accreditation of Laboratory Animal Care International. To establish the tumor-bearing mouse xenograft model, fibrosarcoma HT1080 cells (5×10^6 cells) were implanted into the proximal thigh of female mice (6-week-old BALB/c-nude mice). When the tumor size reached $\sim 500 \text{ mm}^3$, the targeting efficiency of COE to the tumor was investigated by a back injection (40 μL of 50 or 5 μM , respectively) or intravenous injection (40 μL of 5 μM) into the tail vein of the mouse.

2.6. Cytotoxicity and stability test. EPCs, human embryonic kidney 293 cells, and MEFs were plated in 24-well plates. Subsequently, the cells were treated with various concentrations of dyes for 48 h. The cells were then incubated with 1 mg/mL of 3-(4,5-dimethylthiazol-2-yl)-2,5-diphenyltetrazolium bromide (MTT) in the medium for 4 h. The surviving cells were converted to formazan by MTT, forming a blue–purple color when dissolved in dimethyl sulfoxide. The intensity of formazan was measured at 590 nm using a microplate reader. The relative percentage of cell viability was calculated by dividing the absorbance of the treated cells by that of the control sample. FBS was purchased from GIBCO Life Technologies, Carlsbad, CA. To prepare rat plasma, whole blood samples collected from lateral tail vein of 7-week-old male SD (Sprague–Dawley) rats (randomly assigned) were centrifuged at 3 000 rpm for 10 min using a refrigerated centrifuge (4 $^{\circ}\text{C}$). After centrifugation, the nonhemolyzed plasma (yellowish appearance) was properly eluted from the whole blood avoiding disturbing the underlying red and white blood cell layers. The stability of COEs/v was checked with increasing [FBS] (or [rat plasma]) = 1–10 vol % in deionized (DI) water.

2.7. Synthesis. 2-Tributyltin-9,9-bis(6'-bromohexyl)fluorene (4). 2-Bromo-9,9-bis(6'-bromohexyl)fluorene (3) (5.1 g, 8.93 mmol) was dissolved in anhydrous tetrahydrofuran (THF, 40 mL) and cooled to $-78 \text{ }^{\circ}\text{C}$. Subsequently, *n*-butyllithium (in 2.5 M hexane, 3.6 mL, 1 equiv) was added dropwise. After stirring the mixture at $-78 \text{ }^{\circ}\text{C}$ for 1 h, tributyltin chloride (2.1 mL, 1.05 equiv) was added in one portion. The reaction solution was allowed to warm to ambient temperature and stirred overnight. The resulting solution was poured into water and extracted with dichloromethane twice. The combined extract was dried over anhydrous magnesium sulfate, and the solvent was removed under reduced pressure to yield compound 4 as a light yellow oil (6.37 g, 91.2%). Compound 4 was used in the next step without further purification. $^1\text{H NMR}$ (300 MHz, CDCl_3 , δ): 7.62–7.70 (m, 2H), 7.40–7.46 (m, 1H), 7.38 (s, 1H), 7.28–7.34 (m, 3H), 3.26 (t, $J = 6.7 \text{ Hz}$, 4H), 1.96 (t, $J = 8.1 \text{ Hz}$, 4H), 1.51–1.69 (m, 10H), 1.28–1.40 (m, 6H), 1.06–1.23 (m, 14H), 0.85–0.93 (m, 9H), 0.57–0.67 (m, 4H).

2-(9,9-Bis(6'-bromohexyl)fluoren-2-yl)thiophene (5). Into a mixture of 2-bromo-9,9-bis(6'-bromohexyl)fluorene (3) (5.34 g, 9.34 mmol) and $\text{PdCl}_2(\text{PPh}_3)_2$ (328 mg, 5 mol %) was added 40 mL of degassed anhydrous chlorobenzene in a glovebox. Subsequently, 2-(tributylstannyl)thiophene (3.56 mL, 11.2 mmol, 1.2 equiv) was added, and the reaction solution was refluxed overnight. After the solution was cooled down to room temperature, the reaction mixture was poured into water and extracted with dichloromethane. The combined extract was washed with diluted hydrochloric acid and water and dried over anhydrous magnesium sulfate. After removal of the solvent under reduced pressure, the residue was purified by column chromatography on silica gel (dichloromethane/hexane = 1/10, v/v) to give a sticky oil (3.6 g, 67.1%). $^1\text{H NMR}$ (300 MHz, CDCl_3 , δ): 7.67–7.70 (m, 2H), 7.58–7.61 (m, 1H), 7.54 (s, 1H), 7.37–7.39 (m, 1H), 7.28–7.37 (m, 4H), 7.06–7.12 (m, 1H), 3.26 (t, $J = 6.9 \text{ Hz}$, 4H), 2.00 (t, $J = 8.1 \text{ Hz}$, 4H), 1.64 (m, 4H), 1.02–1.26 (m, 8H), 0.60–0.67 (m, 4H). $^{13}\text{C NMR}$ (75 MHz, CDCl_3 , δ): 150.90, 150.25, 144.85, 140.46, 140.41, 133.05, 127.85, 127.00, 126.76, 124.76, 124.32, 122.69, 122.55, 119.90, 119.82, 119.56, 54.81, 40.02, 33.73, 32.39, 28.81, 27.52, 23.28.

2-(5-Tributyltinthiophen-2-yl)-9,9-bis(6'-bromohexyl)fluorene (6). Compound 6 was prepared similarly as described for compound 4. Yield: 82.2%. $^1\text{H NMR}$ (300 MHz, CDCl_3 , δ): 7.66–7.70 (m, 2H), 7.59–7.62 (m, 1H), 7.55 (s, 1H), 7.50 (d, $J = 3.3 \text{ Hz}$, 1H), 7.28–7.36 (m, 3H), 7.16 (d, $J = 3.3 \text{ Hz}$, 1H), 3.26 (t, $J = 6.7 \text{ Hz}$, 4H), 2.00 (t, $J = 8.1 \text{ Hz}$, 4H), 1.57–1.72 (m, 10H), 1.31–1.43 (m, 6H), 1.06–1.26 (m, 14H), 0.83–1.00 (m, 9H), 0.60–0.71 (m, 4H).

4,7-Bis(5-(9,9-bis(6'-bromohexyl)fluoren-2-yl)-thiophen-2-yl)-benzo[2,1,3]thiadiazole (N-FITBTTFI). Compound 2 (758 mg, 2.57 mmol), compound 6 (4.76 g, 6.45 mmol, 2.5 equiv), and $\text{Pd}(\text{PPh}_3)_4$ (356 mg, 0.308 mmol, 12 mol %) were added into 50 mL of degassed chlorobenzene. The mixture was stirred at 100 $^{\circ}\text{C}$ for 36 h. After being cooled to room temperature, the mixture was poured into water and extracted with dichloromethane. The organic layer was washed with brine and water and dried over anhydrous MgSO_4 . After evaporation of the solvent, the residue was purified by column chromatography on silica gel (ethyl acetate/hexane = 1/9, v/v) to afford N-FITBTTFI (2.89 g, 87.5%) as a red solid. $^1\text{H NMR}$ (300 MHz, CDCl_3 , δ): 8.15 (d, $J = 3.6 \text{ Hz}$, 2H), 7.95 (s, 2H), 7.70–7.73 (m, 6H), 7.65 (s, 2H), 7.51 (d, $J = 3.9 \text{ Hz}$, 2H), 7.33–7.36 (m, 6H), 3.28 (t, $J = 6.9 \text{ Hz}$, 8H), 2.01–2.07 (m, 8H), 1.61–1.71 (m, 8H), 1.07–1.26 (m, 16H), 0.65–0.71 (m, 8H). $^{13}\text{C NMR}$ (75 MHz, CDCl_3 , δ): 152.42, 151.03, 150.34, 146.15, 140.92, 140.37, 138.16, 132.78, 128.46, 127.16, 126.82, 125.57, 125.13, 124.70, 123.76, 122.60, 120.02, 119.66, 54.91, 40.07, 33.80, 32.41, 28.83, 27.55, 23.32. MALDI-TOF ($\text{C}_{64}\text{H}_{68}\text{Br}_4\text{N}_2\text{S}_3$): 1282.399 (most abundant mass).

4,8-Bis(5-(9,9-bis(6'-bromohexyl)fluoren-2-yl)benzo[1,2-*c*:4,5-*c'*]bis[1,2,5]thiadiazole (N-FIBBTTFI). Compound 1 (1.10 g, 3.13 mmol), compound 4 (6.37 g, 8.15 mmol, 2.6 equiv), and $\text{Pd}(\text{PPh}_3)_4$ (433 mg, 0.375 mmol, 12 mol %) were dissolved in 50 mL of degassed chlorobenzene and reacted similarly as described for N-FITBTTFI. The crude product was purified by column chromatography on silica gel (ethyl acetate/hexane = 1/9, v/v) to afford N-FIBBTTFI (458 mg, 12.4%) as a blue solid. $^1\text{H NMR}$ (300 MHz, CDCl_3 , δ): 8.28 (d, $J = 6.6 \text{ Hz}$, 4H), 7.97 (d, $J = 8.1 \text{ Hz}$, 2H), 7.82 (d, $J = 6.9 \text{ Hz}$, 2H), 7.33–7.43 (m, 6H), 3.28 (t, $J = 6.7 \text{ Hz}$, 8H), 1.98–2.19 (m, 8H), 1.65–1.74 (m, 8H), 1.32–1.09 (m, 16H), 0.78–0.95 (m, 8H). $^{13}\text{C NMR}$ (75 MHz, CDCl_3 , δ): 153.11, 151.47, 150.35, 141.96, 140.74, 133.99, 130.99, 127.73, 127.18, 123.05, 121.86, 120.37, 119.68, 55.29, 40.17, 34.15, 32.74, 29.23, 27.87, 23.85. MALDI-TOF ($\text{C}_{56}\text{H}_{62}\text{Br}_4\text{N}_4\text{S}_2$): 1178.149.

4,8-Bis(5-(9,9-bis(6'-bromohexyl)fluoren-2-yl)-thiophen-2-yl)-benzo[1,2-*c*:4,5-*c'*]bis[1,2,5]thiadiazole (N-FITBTTFI). Compound 1 (603 mg, 1.71 mmol), compound 6 (3.85 g, 4.45 mmol, 2.6 equiv), and $\text{Pd}(\text{PPh}_3)_4$ (238 mg, 0.21 mmol, 12 mol %) were reacted in 50 mL of degassed chlorobenzene similarly as described for N-FITBTTFI. The crude product was purified by column chromatography on silica gel (dichloromethane/hexane = 1/1, v/v) to afford N-FITBTTFI (327 mg, 14.3%) as a green solid. $^1\text{H NMR}$ (300 MHz, CDCl_3 , δ): 9.08 (d, $J = 4.2 \text{ Hz}$, 2H), 7.83 (d, $J = 8.1 \text{ Hz}$, 2H), 7.72–7.77 (m, 6H), 7.64 (d, $J = 4.2 \text{ Hz}$, 2H), 7.32–7.41 (m, 6H), 3.28 (t, $J = 6.7 \text{ Hz}$, 8H), 2.05–2.13 (m, 8H), 1.62–1.72 (m, 8H), 1.09–1.28 (m, 16H), 0.62–0.75 (m, 8H). $^{13}\text{C NMR}$ (75 MHz, CDCl_3 , δ): 151.08, 151.01, 150.42, 149.70, 141.28, 140.40, 137.11, 133.96, 132.88, 127.29, 126.88, 124.90, 124.13, 122.64, 120.09, 119.75, 113.03, 54.99, 40.11, 33.82, 32.41, 28.85, 27.57, 23.37. MALDI-TOF ($\text{C}_{64}\text{H}_{66}\text{Br}_4\text{N}_4\text{S}_4$): 1340.488.

Synthesis of cationic COEs. 4,7-Bis(5-(9,9-bis(6'-*N,N,N*-trimethylammoniumhexyl)fluoren-2-yl)thiophen-2-yl)benzo[2,1,3]-thiadiazole tetrabromide (Q-FITBTTFI), 4,8-bis(9,9-bis(6'-*N,N,N*-trimethylammoniumhexyl)fluoren-2-yl)benzo[1,2-*c*:4,5-*c'*]bis[1,2,5]-thiadiazole tetrabromide (Q-FIBBTTFI), and 4,8-bis(5-(9,9-bis(6'-*N,N,N*-trimethylammoniumhexyl)fluoren-2-yl)thiophen-2-yl)benzo[1,2-*c*:4,5-*c'*]bis[1,2,5]thiadiazole tetrabromide (Q-FITBTTFI) were prepared by a simple quaternization reaction with trimethylamine in a mixture of THF and methanol. The neutral precursor ($\sim 0.1 \text{ mmol}$) was dissolved in 1 mL of THF, and trimethylamine (25 wt % solution in methanol, 2 mL) was added dropwise with stirring. During reaction, methanol (1 mL) was added to dissolve the precipitated compound every 2 h for 12 h. The reaction mixture was stirred for another 24 h.

After removing the solvent under reduced pressure, the quaternized COEs were precipitated into diethyl ether.

Q-FITBTTFI. Yield: 97.2%. $^1\text{H NMR}$ (300 MHz, CD_3OD , δ): 8.22 (d, $J = 2.0$ Hz, 2H), 8.10 (s, 2H), 7.75–7.85 (m, 8H), 7.62 (d, $J = 1.8$ Hz, 2H), 7.31–7.44 (m, 6H), 3.12–3.20 (m, 8H), 2.98 (s, 36H), 2.07–2.24 (m, 8H), 1.50–1.60 (m, 8H), 1.10–1.25 (m, 16H), 0.65–0.75 (m, 8H).

Q-FIBBTFI. Yield: 89.9%. $^1\text{H NMR}$ (300 MHz, CD_3OD , δ): 8.31–8.38 (m, 4H), 7.99 (d, $J = 8.1$ Hz, 2H), 7.87–7.89 (m, 2H), 7.37–7.51 (m, 6H), 3.14–3.20 (m, 8H), 3.01 (s, 36H), 2.13–2.30 (m, 8H), 1.50–1.62 (m, 8H), 1.15–1.34 (m, 16H), 0.70–1.00 (m, 8H).

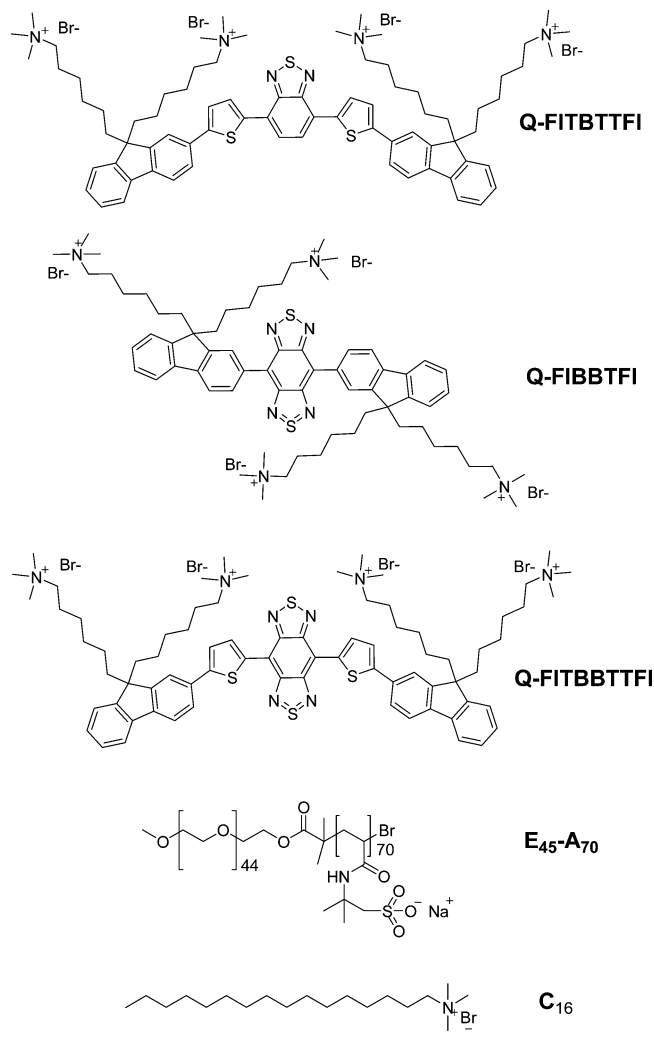
Q-FITBBTTFI. Yield: 99.2%. $^1\text{H NMR}$ (300 MHz, CD_3OD , δ): 9.17 (d, $J = 4.2$ Hz, 2H), 7.76–7.89 (m, 10H), 7.33–7.46 (m, 6H), 3.12–3.17 (m, 8H), 2.98 (s, 36H), 2.15–2.23 (m, 8H), 1.50–1.60 (m, 8H), 1.10–1.28 (m, 16H), 0.65–0.75 (m, 8H).

Synthesis of diblock copolymer ($E_{45}\text{-A}_{70}$). $E_{45}\text{-A}_{70}$ was synthesized via the previous procedures involving an atom transfer radical polymerization (ATRP) of poly(ethylene oxide) macroinitiator ($E_{45}\text{-MI}$) and 2-acrylamido-2-methyl-1-propanesulfonic acid sodium salt (AMPS) with an aid of 2,2'-bipyridine and Cu(I)Cl (yield: 70%).³⁷ The molecular structure and molecular weight of $E_{45}\text{-A}_{70}$ were characterized by $^1\text{H NMR}$ and gel filtration chromatography (GFC). $^1\text{H NMR}$ (300 MHz, D_2O , δ): 4.45 (br, 2H), 4.2–3.8 (m, 181H), 3.8–3.2 (br, 140H), 2.6–2.1 (br, 70H), 2.1–1.0 (br, 566H). The number-average molecular weight (M_n) of the block copolymer was determined to be $18\,000\text{ g mol}^{-1}$ (PDI = 1.73) by GFC in 0.02 M NaNO_3 aqueous solution at $30\text{ }^\circ\text{C}$.

3. RESULT AND DISCUSSION

3.1. Synthesis of water-soluble NIR COEs. Chart 1 and Scheme 1 present the molecular structures and synthetic routes to three types of NIR fluorescent COEs. To decrease the bandgap by modulating the ICT interaction, fluorene (and/or thiophene) was conjugated with benzo[2,1,3]thiadiazole (BT) (or benzo[1,2-*c*:4,5-*c'*]bis[1,2,5]thiadiazole (BBT)) as the electron-rich and -poor units in a molecular framework, respectively. Dibromo-BBT (1) was prepared by a reaction of thionyl bromide and 1,2,4,5-tetraaminobenzene tetrahydrobromide in the presence of pyridine in chloroform.³⁸ The bromination of BT with bromine in hydrobromic acid produced compound 2.³⁹ Compound 3 was synthesized by the alkylation of 2-bromofluorene with 1,6-dibromohexane,⁴⁰ and the successive stannylation with *n*-butyllithium and tributyltin chloride produced compound 4 in 91% yield. Compound 6 was prepared by the Stille coupling of compound 3 and 2-(tributylstannyl)thiophene using $\text{PdCl}_2(\text{PPh}_3)_2$ as a catalyst in chlorobenzene (67% yield), and a successive stannylation reaction by following a similar way for compound 4. The neutral precursors were obtained via Stille coupling using $\text{Pd}(\text{PPh}_3)_4$ as a catalyst in chlorobenzene: 4,7-bis(5-(9,9-bis(6'-bromohexyl)fluoren-2-yl)thiophen-2-yl)benzo[2,1,3]thiadiazole (**N-FITBTTFI**) from 2 and 6 (yield: 87%), 4,8-bis(9,9-bis(6'-bromohexyl)fluoren-2-yl)benzo[1,2-*c*:4,5-*c'*]bis[1,2,5]thiadiazole (**N-FIBBTTFI**) from 1 and 4 (yield: 12%), and 4,8-bis(5-(9,9-bis(6'-bromohexyl)fluoren-2-yl)thiophen-2-yl)benzo[1,2-*c*:4,5-*c'*]bis[1,2,5]thiadiazole (**N-FITBBTTFI**) from 1 and 6 (yield: 14%). The final water-soluble NIR fluorescent COEs, 4,7-bis(5-(9,9-bis(6'-*N,N,N*-trimethylammoniumhexyl)fluoren-2-yl)thiophen-2-yl)benzo[2,1,3]thiadiazole tetrabromide (**Q-FITBTTFI**), 4,8-bis(9,9-bis(6'-*N,N,N*-trimethylammoniumhexyl)fluoren-2-yl)benzo[1,2-*c*:4,5-*c'*]bis[1,2,5]thiadiazole tetrabromide (**Q-FIBBTTFI**), and 4,8-bis(5-(9,9-bis(6'-*N,N,N*-trimethylammoniumhexyl)fluoren-2-yl)thiophen-2-yl)benzo[1,2-*c*:4,5-*c'*]bis[1,2,5]thiadiazole tetrabromide (**Q-FITBBTTFI**) were synthesized in ~95% yield by a

Chart 1. Molecular Structures of NIR COEs, $E_{45}\text{-A}_{70}$, and C_{16}



simple quaternization reaction of the neutral precursors with trimethylamine in a mixed solvent of tetrahydrofuran and methanol at room temperature. A block ionomer, poly[(ethylene oxide)-*block*-(sodium 2-acrylamido-2-methyl-1-propanesulfonate)] ($E_{45}\text{-A}_{70}$), was synthesized using the procedure reported elsewhere (Scheme S1).³⁷ The molecular structures of the intermediates and final compounds were characterized by $^1\text{H NMR}$ spectroscopy, $^{13}\text{C NMR}$ spectroscopy, and MALDI-TOF mass spectroscopy, showing a good agreement with the suggested structures.

3.2. Characterization of neutral precursors. Three kinds of NIR fluorophores with different ICT interactions within the backbone were designed by modulating the D–A molecular combination. As shown in Figure S2, **N-FITBTTFI** shows a clear solvatochromic effect where the λ_{PL} is gradually red-shifted ($\lambda_{\text{PL}} = 646\text{ nm}$ in toluene and 698 nm in dimethyl sulfoxide (DMSO)), indicating a strong ICT interaction. Similarly, **N-FITBBTTFI** shows a red-shifted emission in polar solvents ($\lambda_{\text{PL}} = 1026\text{ nm}$ in toluene and 1086 nm in DMSO). On the contrary, **N-FIBBTTFI** shows a relatively small shift in λ_{PL} with changing solvents, due to weak ICT interaction. In **N-FIBBTTFI**, the fluorene moiety is a weak donor and the resulting ICT is weaker than those in **N-FITBTTFI** and **N-FITBBTTFI** containing the strong donor of thiophene. The PL spectral changes in different solvents are

Scheme 1. Synthetic Routes to Water-Soluble NIR COEs

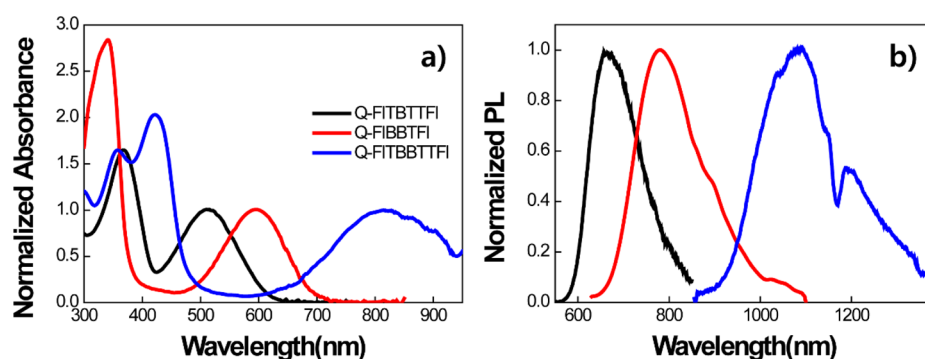
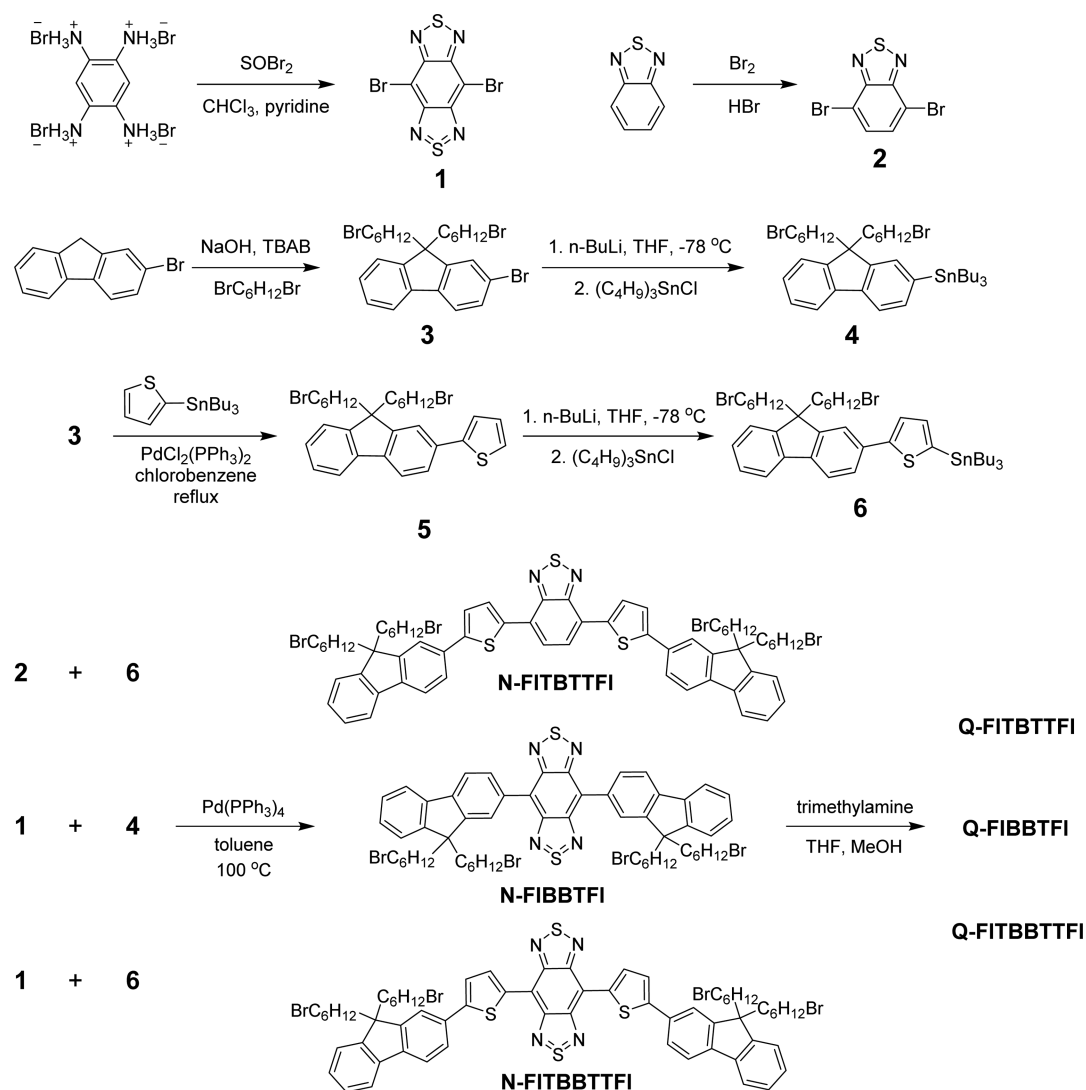


Figure 1. Normalized (a) absorption and (b) PL spectra of cationic NIR fluorescent COEs in water. PL spectrum of Q-FITBBTTFI was measured in DMSO due to low PL quantum yield in water.

summarized in Table S1. In the case of absorption in different solvents, negligible changes were measured in λ_{abs} (compared to PL spectra), because the energy level of ground state (less polar than the excited state) is less sensitive to polarity of solvents (Figure S1). We measured the highest occupied molecular orbital (HOMO)/lowest unoccupied molecular orbital (LUMO) energy levels of N-FITBTTFI, N-FIBBTTFI, and N-FITBBTTFI by cyclic voltammetry (CV) in acetonitrile.

The HOMO/LUMO levels were determined to be $-5.49/-3.50$, $-5.65/-3.78$, and $-5.30/-4.00$ eV for N-FITBTTFI, N-FIBBTTFI, and N-FITBBTTFI, respectively. The electrochemical band gap was determined to be 1.99, 1.88, and 1.30 eV for N-FITBTTFI, N-FIBBTTFI, and N-FITBBTTFI, respectively, suggesting a gradual increase in the ICT interaction with decreased band gap from N-FITBTTFI to N-FITBBTTFI.

3.3. Optical properties of NIR COEs. Figure S3 and Figure 1 present the absorption and PL spectra of the neutral and quaternized NIR fluorophores in toluene and in water, and Table 1 summarizes the optical data. The maximum absorption

Table 1. Summary of Optical Properties of Neutral and Quaternized NIR Fluorophores

compound	solvent	λ_{abs}^a [nm]	λ_{PL}^b [nm]	Φ_{PL}^c [%]	Stokes shift ^d [nm]
N-FITBTTFI	toluene	363, 512	630	77	118
Q-FITBTTFI	water	368, 510	657	5.7	147
N-FIBBTFI	toluene	347, 623	763	55	140
Q-FIBBTFI	water	341, 596	780	3.3	184
N-FITBBTTFI	toluene	424, 838	1022	13.1	184
Q-FITBBTTFI	water	422, 814	~1090	<0.1	~276

^aMaximum absorption wavelength. ^bMaximum PL wavelength. ^c Φ_{PL} (PL quantum efficiency) was measured relative to fluorescein ($\Phi_{\text{PL}} = 92\%$ in water at pH = 10) for N-, Q-FITBTTFI, rhodamine 101 ($\Phi_{\text{PL}} = 96\%$ in methanol) for N-, Q-FIBBTFI, and indocyanine green ($\Phi_{\text{PL}} = 10.6\%$ in DMSO) for N-, Q-FITBBTTFI. ^dStokes shift was estimated by the wavelength difference between λ_{PL} and λ_{abs} .

was measured at $\lambda_{\text{abs}} = 363$ and 512 nm for N-FITBTTFI in toluene and at 368 and 510 nm for Q-FITBTTFI in water. The peak at ~360 nm is attributed to the $\pi \rightarrow \pi^*$ transition, and the peak at a longer wavelength (~510 nm) originates from an ICT interaction.^{41,42} The corresponding emission of N-FITBTTFI in toluene and Q-FITBTTFI in water was observed at $\lambda_{\text{PL}} = 630$ and 657 nm, respectively. By incorporating the stronger acceptor, BBT, in place of BT (N (or Q-FIBBTFI and FITBBTTFI), substantially red-shifted absorption and PL spectra were obtained through the considerably enhanced ICT interactions in a conjugated molecular backbone. In water, the maximum absorption was measured at $\lambda_{\text{abs}} = 341$ and 596 nm for Q-FIBBTFI and $\lambda_{\text{abs}} = 422$ and 814 nm for Q-FITBBTTFI, respectively. The PL spectra were red-shifted further to a range of NIR wavelengths showing $\lambda_{\text{PL}} = 780$ nm and ~1090 nm for Q-FIBBTFI and Q-FITBBTTFI in water, respectively. Because the accepting ability of BBT is much stronger as compared to BT, Q-FITBBTTFI shows the most red-shifted PL at $\lambda_{\text{PL}} \approx 1090$ nm. The strong ICT interaction induced a low bandgap and PL spectra in the NIR range with a large Stokes shift. The Stokes shift for the NIR fluorophores in water (147–276 nm) was substantially larger than those in toluene (118–184 nm). These values are much larger than those (10–30 nm) of cyanine-, BODIPY-, and rhodamine-based commercial NIR fluorescent dyes.⁴³ This large Stokes shift avoids self-quenching and decreases the interference from the excitation backscattered light.^{22,23} Interestingly, an aperture around 1200 nm was measured for N- and Q-FITBBTTFI in toluene and in DMSO. No aperture was observed when the PL spectrum of N-FITBBTTFI was measured in CCl_4 , indicating that its origin may be the second overtone of C–H (1143, 1170, 1195, 1215, and 1225 nm) stretching (Figure S4).⁴⁴

Moderate or high PL quantum efficiency was determined to be 77, 55, and 13.1% for N-FITBTTFI, N-FIBBTFI, and N-FITBBTTFI, respectively, in toluene (Table 1). In water, the PL efficiency for Q-FITBTTFI, Q-FIBBTFI, and Q-FITBBTTFI was decreased significantly to 5.7, 3.3, and ~0.1%, respectively, due to ICT-related quenching with an increase in the nonradiative decay rate in highly polar media

(energy gap law).^{45,46} The poor PL efficiency is a common problem for NIR fluorophores in water that needs to be overcome to allow bioimaging with high resolution. To improve the PL efficiency of the NIR dyes in water, a vesicular complex containing the NIR COE was also prepared, where the microenvironment near the COE is hydrophobic (similar to organic media) and the PL efficiency of NIR COEs is expected to increase. The block ionomer, $\text{E}_{45}\text{-A}_{70}$, was prepared according to the previously reported procedure.³⁷ The polymer vesicle containing the NIR COE was self-organized via electrostatic and hydrophobic/hydrophilic interactions among the cationic NIR COE, anionic $\text{E}_{45}\text{-A}_{70}$, and cationic surfactant C_{16} (Scheme S1). Positively charged COEs undergo electrostatic adhesion onto the anionic block of $\text{E}_{45}\text{-A}_{70}$. Similarly, the cationic C_{16} molecules form the electrostatic complexes with the remaining negative sulfonate groups in $\text{E}_{45}\text{-A}_{70}$. As the net charge becomes zero, the ionic blocks are neutralized to be hydrophobic and the hydrophilic poly(ethylene oxide) blocks (in the other block of $\text{E}_{45}\text{-A}_{70}$) surround it, resulting in the vesicular structure. The hydrophobic vesicular membrane is formed via electrostatic and hydrophobic interactions of cationic C_{16} and anionic sulfonate groups in $\text{E}_{45}\text{-A}_{70}$. The cationic COE is also located inside the membrane where the positive ammonium groups show the electrostatic complexation with anionic sulfonate groups in $\text{E}_{45}\text{-A}_{70}$. Finally, the hydrophilic poly(ethylene oxide) blocks on the outer and inner surfaces of the vesicle stabilize the vesicular structure in aqueous media. The detailed synthesis and characterization data (including zeta potential and transmission electron microscope images) were reported in our previous report.³⁷ By forming the vesicular complexes (NIR COE/v), the PL intensity increased greatly (Figure 2). The PL quantum efficiency increased substantially (by 5–10 times), up to 27.8, 13.4, and 1.2% for Q-FITBTTFI, Q-FIBBTFI, and Q-FITBBTTFI in water, respectively (Table S2). The mean size of the vesicles was measured to be ~68 nm (in diameter) by dynamic light scattering (Figure S5). The vesicular complex might have additional advantages, i.e., the ability to encapsulate hydrophilic and hydrophobic drug molecules, biocompatibility, easy preparation, and controllable size, suggesting further extended multifunctional biological applications for drug delivery systems, etc.^{47–49}

3.4. In vitro cell imaging by single-photon and two-photon fluorescence microscopy. To evaluate the applications of the water-soluble NIR COEs to the visualization of cells, single- and two-photon excited fluorescence-imaging experiments were performed after incubating endothelial progenitor cells (EPCs) with 10 μM NIR fluorescent Q-FITBTTFI and Q-FIBBTFI for 12 h. Fluorescence imaging with Q-FITBBTTFI could not be tested because no commercial imaging instrument covering its PL spectral range ($\lambda_{\text{PL}} \approx 1090$ nm) was available. The fluorescence images of EPCs were collected by both confocal single-photon fluorescence microscopy (excited at 514 or 712 nm) and two-photon fluorescence microscopy (excited at ~1100 nm) (Figure 3). Two-photon microscopy has several advantages over its single-photon counterpart including negligible background due to cellular autofluorescence, better spatial resolution, larger penetration depth, reduced photodamage, and ability to image turbid samples.^{50–52} In single-photon fluorescence microscopy, EPCs were clearly visualized via staining of intracellular structures by both Q-FITBTTFI and Q-FIBBTFI, suggesting their potential as fluorescent tags for

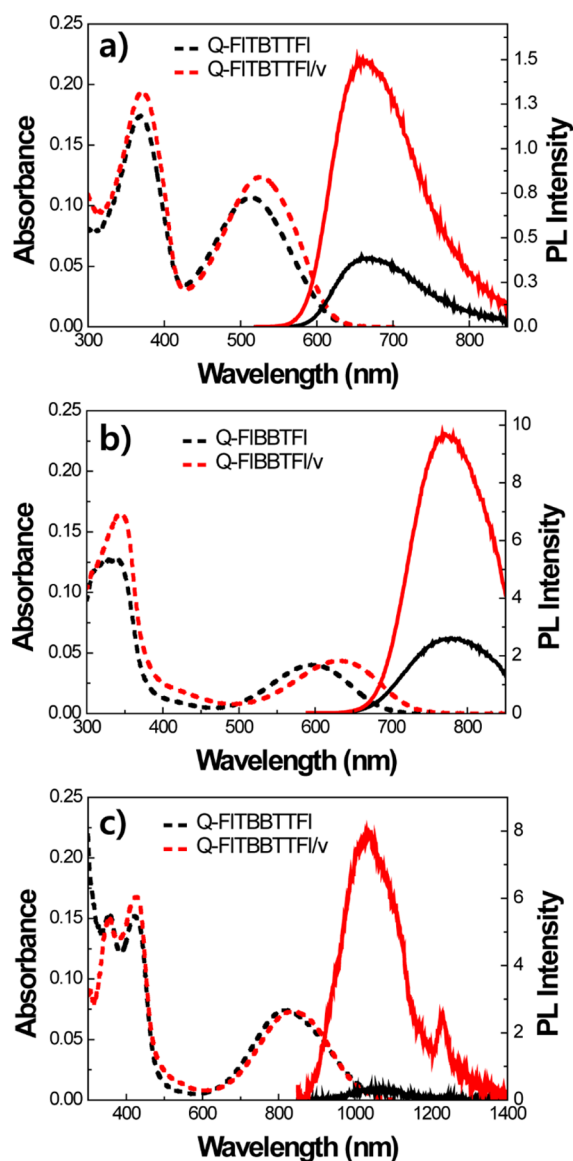


Figure 2. Absorption (dashed) and PL (solid) spectra of (a) Q-FITBTTFI, (b) Q-FITBTTFI, and (c) Q-FITBBTTFI (black) and their vesicular complexes (red) in water.

molecular probes. In two-photon fluorescence microscopy with EPCs, Q-FITBTTFI showed two-photon induced signals and

generated similar images with those from single-photon confocal fluorescence microscopy (Figure 3b). On the other hand, Q-FIBBTTFI did not generate a detectable signal with two-photon fluorescence microscopy. These results suggest that both Q-FITBTTFI and Q-FIBBTTFI are cell-permeable with low cytotoxicity (detailed data will be discussed in the following section) and can be used for visualizing cells with fluorescence microscopy. In addition, Q-FITBTTFI can be utilized as a fluorescent tag for bioimaging with two-photon fluorescence microscopy.

3.5. In vivo and ex vivo fluorescence imaging. To further evaluate the in vivo fluorescence imaging capability of the synthesized COEs, the in vivo fluorescence signals of Q-FIBBTTFI and Q-FIBBTTFI/v were collected in the back of mouse model by injecting the NIR COEs (50 μ M) subcutaneously into the back region of a BALB/c nude mouse (Figure 4). Q-FIBBTTFI and Q-FIBBTTFI/v were chosen as the NIR imaging probe because of its adequate PL wavelength for in vivo imaging. The fluorescence signal at the Q-FIBBTTFI/v-injected site (right back side of the mouse in Figure 4a) showed \sim 4 times higher intensity than the Q-FIBBTTFI-injected site (left back side of mouse) in 10 min after the injection. The COE/v complex showed much brighter PL emission in a mouse model, suggesting its great potential as a NIR fluorescent agent for in vivo optical imaging with high imaging resolution. Therefore, further in vivo imaging experiments were conducted using Q-FIBBTTFI/v to evaluate its capability as an in vivo NIR imaging probe. Human fibrosarcoma HT1080 cells were transplanted into the proximal thigh region of a BALB/c nude mouse to prepare the tumor-bearing xenograft mouse model. After implanting the HT1080 cells, the vesicular complex (Q-FIBBTTFI/v) was injected intravenously into the tail vein of the xenograft mouse model and NIR in vivo images were taken using an in vivo optical imager. The NIR fluorescence signal at the tumor site was enhanced by \sim 20 times compared to the signal intensity of the preinjection state (Figure 4c and d). The PL signal was maximized at 30 min after injection. Although there was no targeting moiety conjugated to the COE/v, such as an antibody, aptamer, and peptide, the strongest fluorescence signal was detected at the tumor region due to the enhanced permeability and retention (EPR) effect.^{53–55} The EPR effect is related to the cell structures of fast growing tumors compared to normal cells, showing efficient accumulation of molecules in tumor. The tumor has an abnormally high density of angiogenic blood vessels for the violent supply of nutrients for the growth

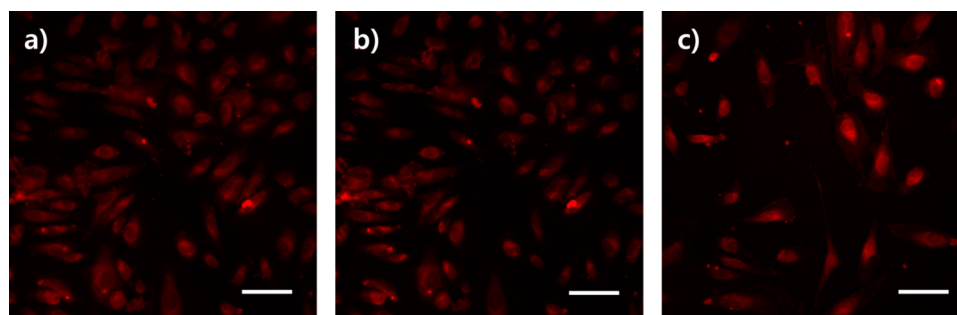


Figure 3. Fluorescence microscope images of EPCs. (a) Confocal single-photon and (b) two-photon microscope images of EPCs after incubation with 10 μ M of Q-FITBTTFI for 12 h. The wavelengths for single-photon and two-photon excitation were 514 nm and 1100 nm, respectively. (c) Confocal single-photon microscope image of EPCs after incubation with 10 μ M of Q-FIBBTTFI for 12 h. The excitation wavelength was 712 nm. Scale bar is 50 μ m.

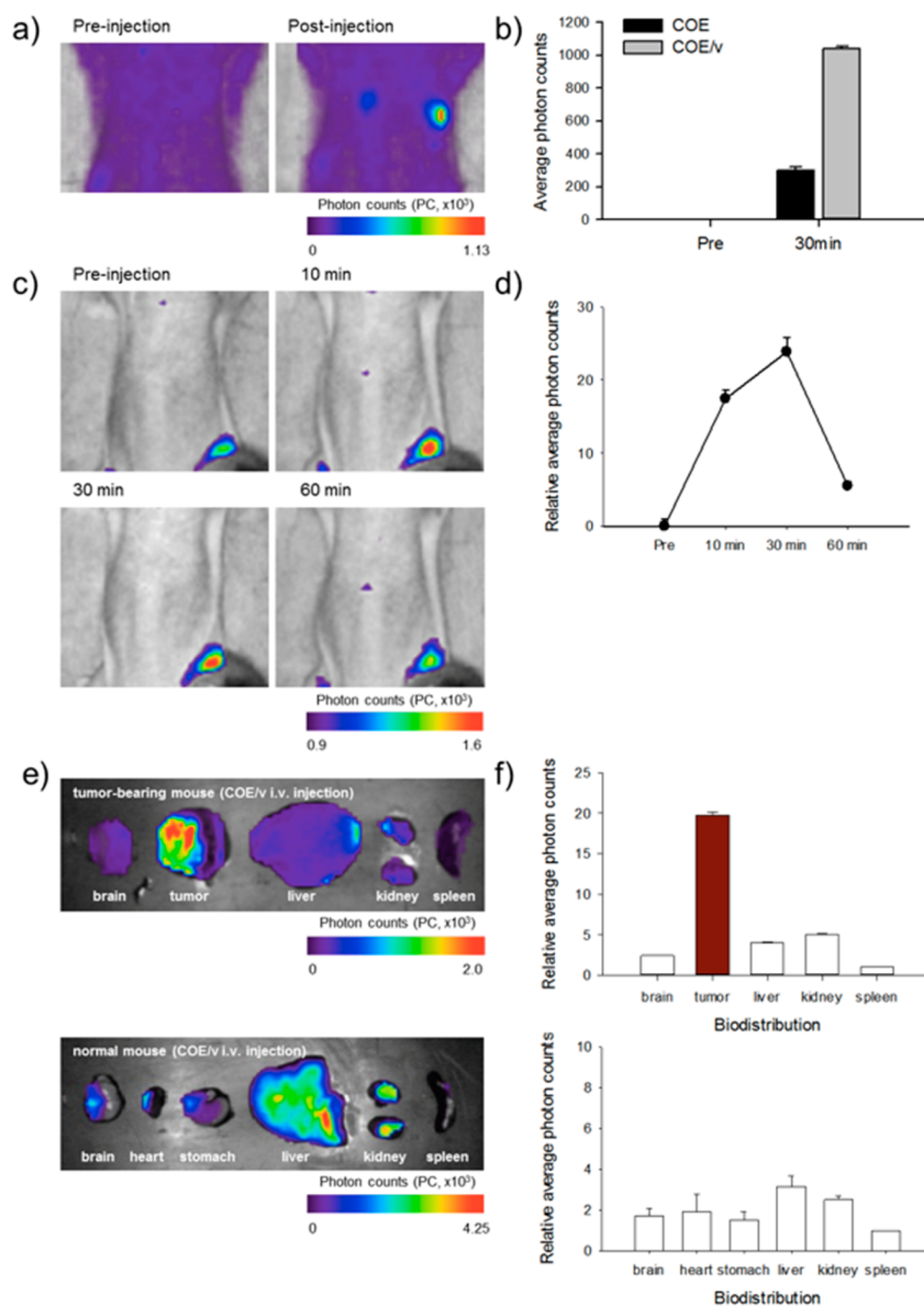


Figure 4. (a) In vivo fluorescence images and (b) a graph of average photon counts for the injected back sites of Q-FIBBTfI (left) and Q-FIBBTfI/v (right). (c) In vivo fluorescence images and (d) a graph of relative photon counts in tumor-bearing mouse model after intravenous injection of Q-FIBBTfI/v into tail vein. (e) Ex vivo fluorescence image and (f) a graph of relative average photon counts of indicated tissues after intravenous injection of Q-FIBBTfI/v for 1 h; tumor-bearing mouse (upper) and normal mouse (lower).

and proliferation of cancerous cells.⁵⁶ In addition, the general absence of functional lymphatic vessels in most tumors contributes to nanocarrier entrapment and retention. Thus, in the last few decades, EPR effect has been considered the “royal gate” for cancer control because bionanoparticles can be accumulated inside a tumor and reduce the side effects compared to conventional treatments.⁵⁷ The fundamental features of EPR physiology are ascribed to hyperpermeable vasculatures in tumors, allowing the concentration and the decrease of a renal clearance of bionanoparticles. Thus, our

nanoscale Q-FIBBTfI/v might be extravasated and accumulated within the interstitial space of tumors by transiting through submicroscale endothelial pores. As shown in Figure 4e and f, the ex vivo image of the tumor treated with the Q-FIBBTfI/v demonstrates a substantially higher fluorescence signal than the other organs, such as the brain, liver, kidney, and spleen. These results strongly suggest that the Q-FIBBTfI/v has great potential as a NIR imaging probe for the diagnosis of cancer. Furthermore, the utility of the Q-FIBBTfI/v can be extended to molecular bioprobes for the quantification of

tumors and for targeting a specific type of tumor by conjugation with the targeting ligands.

3.6. Cytotoxicity and stability test. To test the cytotoxicity of the NIR COEs, EPCs, human embryonic kidney 293 cells (293 cells) and MEFs were treated with different concentrations of Q-FITBTTFI or Q-FIBBTFI (1 μM –1 mM, 37 $^{\circ}\text{C}$, 24 h) and subjected to a MTT assay. At concentrations of 10 μM or lower, neither Q-FITBTTFI nor Q-FIBBTFI affected the viability of tested cells (Figure 5). However, at 100

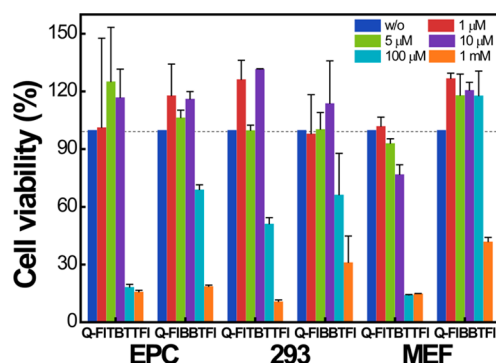


Figure 5. Cell viability in the presence of NIR COEs. EPCs, 293 cells, and MEFs were subjected to MTT assay after incubation with different concentrations of Q-FITBTTFI or Q-FIBBTFI (1 μM –1 mM) at 37 $^{\circ}\text{C}$ for 24 h.

μM and higher concentrations, Q-FITBTTFI and Q-FIBBTFI decreased the cellular viability compared with the untreated controls. Little subcellular apoptotic changes or significant cell death were observed at the concentrations used for in vitro (10 μM) or in vivo (50 μM) visualization. These results suggest that Q-FITBTTFI and Q-FIBBTFI can be applied for visualizing cells in vitro and tumors in vivo with low cytotoxicity when used within a certain range of concentrations. We also tested the stability of Q-FITBTTFI/v and Q-FIBBTFI/v in FBS and in rat plasma by measuring PL intensity change with increasing [FBS] (or [rat plasma]) = 1–10 vol % in DI water (Figure 6). Both COE/v structures show almost no decrease in the PL intensity up to the addition of 5 vol % of FBS or rat plasma in water. The fluorescence was substantially decreased to approximately half of the original PL signal in the presence of 10 vol % of FBS or rat plasma. The COE/v may show nonspecific adhesion onto proteins, antibodies, etc. in blood serum and the structure might be changed, inducing PL quenching.

4. CONCLUSION

Three kinds of water-soluble fluorescent conjugated oligoelectrolytes (COEs) were designed and synthesized as a NIR fluorescence imaging agent. The cationic ammonium groups were attached to their side-chains, and the emission wavelength was modulated by adjusting the intramolecular charge transfer interaction by incorporating the electron-rich fluorene (and/or thiophene) and electron-poor BT (or BBT) moieties in their molecular framework. The COEs showed PL spectra in the range 600–1300 nm, with a remarkably larger Stokes shift (147–276 nm) compared to commercial rhodamine and cyanine dyes in water, avoiding self-quenching and interference from the excitation backscattered light. The PL quantum efficiency was improved substantially (1.2–27.8% in water) by incorporating the COEs in a polymeric vesicle. In particular, Q-

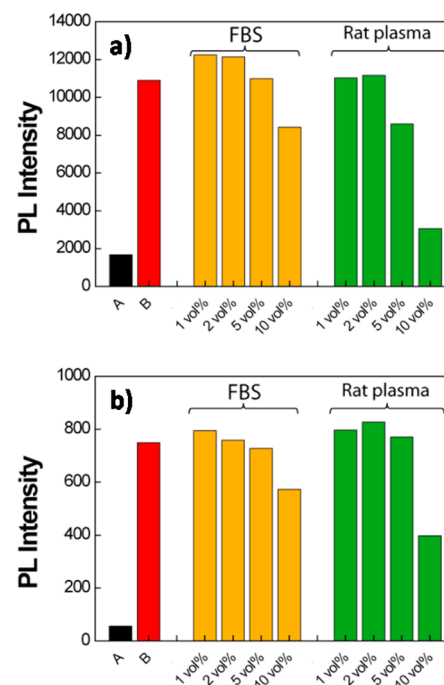


Figure 6. PL intensity of (a) Q-FITBTTFI/v and (b) Q-FIBBTFI/v by varying [FBS] or [blood serum] = 1–10 vol % in water. [COE] = [E_{45-A70}] = 5 μM . [C₁₆] = 375 μM . Enhanced PL intensity (PL intensity of COE itself: A, black) was observed by forming the vesicular structure of COE/v (B, red). PL intensity was compared at the maximum emission wavelength.

FITBTTFI and Q-FIBBTFI showed good biodistribution and low cytotoxicity and successfully demonstrated their potential in in vitro confocal microscopy. In addition, the Q-FIBBTFI/v exhibited great potential as an in vivo biological imaging agent for the mouse xenograft model. Significant opportunities and great challenges in the development of water-soluble NIR COEs still remain. The application of COEs can be further extended to active targeting and the delivery of therapeutics by conjugation with specific ligands, such as small molecules, peptides, proteins, and antibodies.

■ ASSOCIATED CONTENT

Supporting Information

The Supporting Information is available free of charge on the ACS Publications website at DOI: 10.1021/acsami.6b04276.

Synthetic scheme, additional optical, DLS data, and MALDI-TOF and H NMR spectra (PDF)

■ AUTHOR INFORMATION

Corresponding Authors

*J. Yang e-mail: 177hum@yuhs.ac.

*J. H. Kim e-mail: jhkimst@pusan.ac.kr.

*H. Y. Woo e-mail: hywoo@korea.ac.kr.

Author Contributions

S.-J.W., S.P., and J.-E.J. contributed equally.

Funding

We are grateful for financial support from the National Research Foundation (NRF) of Korea (2015R1A2A1A15055605, 2015R1D1A1A09056905, and 20100020209).

Notes

The authors declare no competing financial interest.

REFERENCES

- (1) Lichtman, J. W.; Conchello, J.-A. Fluorescence Microscopy. *Nat. Methods* **2005**, *2*, 910–919.
- (2) Kobayashi, H.; Ogawa, M.; Alford, R.; Choyke, P. L.; Urano, Y. New Strategies for Fluorescent Probe Design in Medical Diagnostic Imaging. *Chem. Rev.* **2010**, *110*, 2620–2640.
- (3) Chen, X.; Tian, X.; Shin, I.; Yoon, J. Yoon, Fluorescent and luminescent probes for detection of reactive oxygen and nitrogen species. *Chem. Soc. Rev.* **2011**, *40*, 4783–4804.
- (4) Fan, J.; Hu, M.; Zhan, P.; Peng, X. Energy Transfer Cassettes based on Organic Fluorophores: Construction and Applications in Ratiometric Sensing. *Chem. Soc. Rev.* **2013**, *42*, 29–43.
- (5) Choi, H. S.; Gibbs, S. L.; Lee, J. H.; Kim, S. H.; Ashitate, Y.; Liu, F.; Hyun, H.; Park, G.; Xie, Y.; Bae, S.; Henary, M.; Frangioni, J. V. Targeted Zwitterionic Near-Infrared Fluorophores for Improved Optical Imaging. *Nat. Biotechnol.* **2013**, *31*, 148–153.
- (6) Kaloyanova, S.; Zagranyarski, Y.; Ritz, S.; Hanulová, M.; Koynov, K.; Vonderheit, A.; Müllen, K.; Peneva, K. Water-Soluble NIR-Absorbing Rylene Chromophores for Selective Staining of Cellular Organelles. *J. Am. Chem. Soc.* **2016**, *138*, 2881–2884.
- (7) Wickham, A.; Sjölander, D.; Bergström, G.; Wang, E.; Rajendran, V.; Hildesjö, C.; Skoglund, K.; Nilsson, K. P. R.; Aili, D. Near-Infrared Emitting and Pro-Angiogenic Electrospun Conjugated Polymer Scaffold for Optical Biomaterial Tracking. *Adv. Funct. Mater.* **2015**, *25*, 4274–4281.
- (8) Weissleder, R.; Tung, C. H.; Mahmood, U.; Bogdanov, A., Jr In Vivo Imaging of Tumors with Protease-Activated Near-Infrared Fluorescent Probes. *Nat. Biotechnol.* **1999**, *17*, 375–378.
- (9) Frangioni, J. V. In Vivo Near-Infrared Fluorescence Imaging. *Curr. Opin. Chem. Biol.* **2003**, *7*, 626–634.
- (10) Gioux, S.; Choi, H. S.; Frangioni, J. V. Image-Guided Surgery using Invisible Near-Infrared Light: Fundamentals of Clinical Translation. *Mol. Imaging* **2010**, *9*, 237–255.
- (11) Lim, S.-Y.; Hong, K.-H.; Kim, D. I.; Kwon, H.; Kim, H.-J. Tunable Heptamethine–Azo Dye Conjugate as an NIR Fluorescent Probe for the Selective Detection of Mitochondrial Glutathione over Cysteine and Homocysteine. *J. Am. Chem. Soc.* **2014**, *136*, 7018–7025.
- (12) Wu, X.; Sun, X.; Guo, Z.; Tang, J.; Shen, Y.; James, T. D.; Tian, H.; Zhu, W. In Vivo and in Situ Tracking Cancer Chemotherapy by Highly Photostable NIR Fluorescent Theranostic Prodrug. *J. Am. Chem. Soc.* **2014**, *136*, 3579–3588.
- (13) Li, Y.; Sun, Y.; Li, J.; Su, Q.; Yuan, W.; Dai, Y.; Han, C.; Wang, Q.; Feng, W.; Li, F. Ultrasensitive Near-Infrared Fluorescence-Enhanced Probe for in Vivo Nitroreductase Imaging. *J. Am. Chem. Soc.* **2015**, *137*, 6407–6416.
- (14) Yuan, L.; Lin, W.; Zheng, K.; He, L.; Huang, W. Far-Red to Near Infrared Analyte-Responsive Fluorescent Probes based on Organic Fluorophore Platforms for Fluorescence Imaging. *Chem. Soc. Rev.* **2013**, *42*, 622–661.
- (15) Wang, T.; Zhao, Q.-J.; Hu, H.-G.; Yu, S.-C.; Liu, X.; Liu, L.; Wu, Q.-Y. Spirolactonized Si-Rhodamine: a Novel NIR Fluorophore utilized as a Platform to Construct Si-Rhodamine-based Probes. *Chem. Commun.* **2012**, *48*, 8781–8783.
- (16) Cao, X.; Lin, W.; Wan, W. Development of a Near-Infrared Fluorescent Probe for Imaging of Endogenous Cu⁺ in Live Cells. *Chem. Commun.* **2012**, *48*, 6247–6249.
- (17) Koide, Y.; Urano, Y.; Hanaoka, K.; Piao, W.; Kusakabe, M.; Saito, N.; Terai, T.; Okabe, T.; Nagano, T. Development of NIR Fluorescent Dyes Based on Si-rhodamine for in Vivo Imaging. *J. Am. Chem. Soc.* **2012**, *134*, 5029–5031.
- (18) Jiang, X.-D.; Gao, R.; Yue, Y.; Sun, G.-T.; Zhao, W. A NIR BODIPY Dye Bearing 3,4,4a-Trihydroxanthene Moieties. *Org. Biomol. Chem.* **2012**, *10*, 6861–6865.
- (19) Johnson, J. R.; Fu, N.; Arunkumar, E.; Leevy, W. M.; Gammon, S. T.; Piwnica-Worms, D.; Smith, B. D. Squaraine Rotaxanes: Superior Substitutes for Cy-5 in Molecular Probes for Near-Infrared Fluorescence Cell Imaging. *Angew. Chem., Int. Ed.* **2007**, *46*, 5528–5531.
- (20) Wang, X.; Cui, L.; Zhou, N.; Zhu, W.; Wang, R.; Qian, X.; Xu, Y. A Highly Selective and Sensitive Near-Infrared Fluorescence Probe for Arylamine N-acetyltransferase 2 in Vitro and in Vivo. *Chem. Sci.* **2013**, *4*, 2936–3940.
- (21) Sun, Y.-Q.; Liu, J.; LV, X.; Liu, Y.; Zhao, Y.; Guo, W. Rhodamine-inspired Far-Red to Near-Infrared Dyes and their Application as Fluorescence Probes. *Angew. Chem., Int. Ed.* **2012**, *51*, 7634–7636.
- (22) Tolosa, L.; Nowaczyk, K.; Lakowicz, J. In *An introduction to laser spectroscopy*, 2nd ed.; Andrews, D. L., Demidov, A. A., Eds.; Kluwer: New York, 2002; Ch. 5.
- (23) Achilefu, S. The Insatiable Quest for Near-Infrared Fluorescent Probes for Molecular Imaging. *Angew. Chem., Int. Ed.* **2010**, *49*, 9816–9818.
- (24) Luo, S.; Zhang, E.; Su, Y.; Cheng, T.; Shi, C. A Review of NIR Dyes in Cancer Targeting and Imaging. *Biomaterials* **2011**, *32*, 7127–7138.
- (25) Yang, R.; Xu, Y.; Dang, X.-D.; Nguyen, T.-Q.; Cao, Y.; Bazan, G. C. Conjugated Oligoelectrolyte Electron Transport/Injection Layers for Organic Optoelectronic Devices. *J. Am. Chem. Soc.* **2008**, *130*, 3282–3283.
- (26) Pu, K.-Y.; Li, K.; Zhang, X.; Liu, B. Conjugated Oligoelectrolyte Harnessed Polyhedral Oligomeric Silsesquioxane as Light-Up Hybrid Nanodot for Two-Photon Fluorescence Imaging of Cellular Nucleus. *Adv. Mater.* **2010**, *22*, 4186–4189.
- (27) Ding, D.; Pu, K.; Li, K.; Liu, B. Conjugated Oligoelectrolyte-Polyhedral Oligomeric Silsesquioxane loaded pH-Responsive Nanoparticles for Targeted Fluorescence Imaging of Cancer Cell Nucleus. *Chem. Commun.* **2011**, *47*, 9837–9839.
- (28) Herland, A.; Nilsson, K. P. R.; Olsson, J. D. M.; Hammarström, P.; Konradsson, P.; Inganäs, O. Synthesis of a Regioregular Zwitterionic Conjugated Oligoelectrolyte, Usable as an Optical Probe for Detection of Amyloid Fibril Formation at Acidic pH. *J. Am. Chem. Soc.* **2005**, *127*, 2317–2323.
- (29) Duarte, A.; Chworos, A.; Flagan, S. F.; Hanrahan, G.; Bazan, G. C. Identification of Bacteria by Conjugated Oligoelectrolyte/Single-Stranded DNA Electrostatic Complexes. *J. Am. Chem. Soc.* **2010**, *132*, 12562–12564.
- (30) Liang, J.; Li, K.; Gurzadyan, G. G.; Lu, X.; Liu, B. Silver Nanocube-Enhanced Far-Red/Near-Infrared Fluorescence of Conjugated Polyelectrolyte for Cellular Imaging. *Langmuir* **2012**, *28*, 11302–11309.
- (31) Ellinger, S.; Graham, K. R.; Shi, P.; Farley, R. T.; Steckler, T. T.; Brookins, R. N.; Taranekar, P.; Mei, J.; Padilha, L. A.; Ensley, T. R.; Hu, H.; Webster, S.; Hagan, D. J.; Van Stryland, E. W.; Schanze, K. S.; Reynolds, J. R. Donor–Acceptor–Donor-based π -Conjugated Oligomers for Nonlinear Optics and Near-IR Emission. *Chem. Mater.* **2011**, *23*, 3805–3817.
- (32) Thomas, A. W.; Henson, Z. B.; Du, J.; Vandenberg, C. A.; Bazan, G. C. Synthesis, Characterization, and Biological Affinity of a Near-Infrared-Emitting Conjugated Oligoelectrolyte. *J. Am. Chem. Soc.* **2014**, *136*, 3736–3739.
- (33) Tang, T.; Lin, T.; Wang, F.; He, C. Origin of Near-Infrared Absorption for Azulene-Containing Conjugated Polymers upon Protonation or Oxidation. *J. Phys. Chem. B* **2015**, *119*, 8176–8183.
- (34) Kim, S.; Pudavar, H. E.; Bonoiu, A.; Prasad, P. N. Aggregation-Enhanced Fluorescence in Organically Modified Silica Nanoparticles: A Novel Approach toward High-Signal-Output Nanoprobes for Two-Photon Fluorescence Bioimaging. *Adv. Mater.* **2007**, *19*, 3791–3795.
- (35) Ma, Y.; Sheng, Y.; Tang, C.; Hong, X.; Chen, S. C.; Zhu, D.; Zheng, Q. Indenofluorene based Water Soluble Conjugated Oligomers for Hg²⁺ Detection. *Sens. Actuators, B* **2013**, *176*, 132–140.
- (36) Turro, N. J. *Modern Molecular Photochemistry*; University Science Books: Sausalito, CA, 1991.
- (37) Nag, O. K.; Lim, C. S.; Nguyen, B. L.; Kim, B.; Jang, J.; Han, J. H.; Cho, B. R.; Woo, H. Y. pH-Responsive Water Soluble Smart

Vesicles containing a Bis(styryl)benzene Derivative for Two-Photon Microscopy Imaging. *J. Mater. Chem.* **2012**, *22*, 1977–1984.

(38) Tam, T. L.; Li, H.; Wei, F.; Tan, K. J.; Kloc, C.; Lam, Y. M.; Mhaisalkar, S. G.; Grimsdale, A. C. One-Pot Synthesis of 4,8-Dibromobenzo[1,2-c;4,5-c']bis[1,2,5]thiadiazole. *Org. Lett.* **2010**, *12*, 3340–3343.

(39) Liu, B.; Bazan, G. C. Synthesis of Cationic Conjugated Polymers for Use in Label-Free DNA Microarrays. *Nat. Protoc.* **2006**, *1*, 1698–1702.

(40) Liu, B.; Gaylord, B. S.; Wang, S.; Bazan, G. C. Effect of Chromophore-Charge Distance on the Energy Transfer Properties of Water-Soluble Conjugated Oligomers. *J. Am. Chem. Soc.* **2003**, *125*, 6705–6714.

(41) Amthor, S.; Lambert, C.; Dümmler, S.; Fischer, I.; Schelter, J. Excited Mixed-Valence States of Symmetrical Donor–Acceptor–Donor π Systems. *J. Phys. Chem. A* **2006**, *110*, 5204–5214.

(42) Qian, G.; Dai, B.; Luo, M.; Yu, D.; Zhan, J.; Zhang, Z.; Ma, D.; Wang, Z. Y. Band Gap Tunable, Donor–Acceptor–Donor Charge-Transfer Heteroquinoid-Based Chromophores: Near Infrared Photoluminescence and Electroluminescence. *Chem. Mater.* **2008**, *20*, 6208–6216.

(43) Yuan, A.; Wu, J.; Tang, X.; Zhao, L.; Xu, F.; Hu, Y. Application of Near-Infrared Dyes for Tumor Imaging, Photothermal, and Photodynamic Therapies. *J. Pharm. Sci.* **2013**, *102*, 6–28.

(44) Shenk, J. S.; Workman, J. J., Jr.; Westerhaus, M. O. In *Handbook of Near-Infrared Analysis*, 3rd ed.; Burns, D. A., Ciurczak, E. W., Eds.; CRC Press: Boca Raton, FL, 2007; Ch. 17.

(45) Doroshenko, A. O.; Bilokin, M. D.; Pivovarenko, V. G. New Fluorescent Dye of Dibenzalicyclopentanone Series Possessing Increased Solvatochromism and “Energy Gap Law” Regulated Fluorescence Quenching in Polar Solvents. *J. Photochem. Photobiol., A* **2004**, *163*, 95–102.

(46) Cheng, Y.; Doane, T. L.; Chuang, C.-H.; Ziady, A.; Burda, C. Near Infrared Light-Triggered Drug Generation and Release from Gold Nanoparticle Carriers for Photodynamic Therapy. *Small* **2014**, *10*, 1799–1804.

(47) Discher, B. M.; Won, Y. Y.; Ege, D. S.; Lee, J. C.; Bates, F. S.; Discher, D. E.; Hammer, D. A. Polymersomes: Tough Vesicles made from Diblock Copolymers. *Science* **1999**, *284*, 1143–1146.

(48) Zhou, S.; Chu, B. Assembled Materials: Polyelectrolyte–Surfactant Complexes. *Adv. Mater.* **2000**, *12*, 545–556.

(49) Qin, S.; Geng, Y.; Discher, D. E.; Yang, S. Temperature-Controlled Assembly and Release from Polymer Vesicles of Poly-(ethylene oxide)-block-poly(N-isopropylacrylamide). *Adv. Mater.* **2006**, *18*, 2905–2909.

(50) Denk, W.; Strickler, J. H.; Webb, W. W. Two-Photon Laser Scanning Fluorescence Microscopy. *Science* **1990**, *248*, 73–76.

(51) So, P. T. C.; Dong, C. Y.; Masters, B. R.; Berland, K. M. Two-Photon Excitation Fluorescence Microscopy. *Annu. Rev. Biomed. Eng.* **2000**, *2*, 399–429.

(52) Helmchen, F.; Denk, W. Deep Tissue Two-Photon Microscopy. *Nat. Methods* **2005**, *2*, 932–940.

(53) Duncan, R. Polymer Conjugates for Tumour Targeting and Intracytoplasmic Delivery. The EPR Effect as a Common Gateway? *Pharm. Sci. Technol. Today* **1999**, *2*, 441–449.

(54) Maeda, H.; Wu, J.; Sawa, T.; Matsumura, Y.; Hori, K. Tumor Vascular Permeability and the EPR Effect in Macromolecular Therapeutics: a Review. *J. Controlled Release* **2000**, *65*, 271–284.

(55) Wu, X.; He, X.; Wang, K.; Xie, C.; Zhou, B.; Qing, Z. Qing, Ultrasmall Near-Infrared Gold Nanoclusters for Tumor Fluorescence Imaging in Vivo. *Z. Nanoscale* **2010**, *2*, 2244–2249.

(56) Matsumura, Y.; Maeda, H. A New Concept for Macromolecular Therapeutics in Cancer Chemotherapy: Mechanism of Tumoritropic Accumulation of Proteins and the Antitumor Agent Smancs. *Cancer Res.* **1986**, *46*, 6387–6392.

(57) Nichols, J. W.; Bae, Y. H. EPR: Evidence and Fallacy. *J. Controlled Release* **2014**, *190*, 451–464.